Molecular Catalysis 498 (2020) 111241

Contents lists available at ScienceDirect

Molecular Catalysis

journal homepage: www.journals.elsevier.com/molecular-catalysis

Metal-Organic frameworks-derived multifunctional carbon encapsulated metallic nanocatalysts for catalytic peroxymonosulfate activation and electrochemical hydrogen generation

Md Ariful Ahsan [a,c,*], Alain R. Puente Santiago [a], Aruna Narayanan Nair [a], J. Mark Weller [b], Mohammed F. Sanad [d], Delia J. Valles-Rosales [e], Candace K. Chan [b,c], Sreeprasad Sreenivasan [a,*], Juan C. Noveron [a,c,*]

[a] Department of Chemistry, University of Texas at El Paso, El Paso, TX, USA
[b] Materials Science and Engineering, School for Engineering of Matter, Transport and Energy, Arizona State University, Tempe, AZ, USA
[c] Nanosystems Engineering Research Center for Nanotechnology-Enabled Water Treatment, USA
[d] Department of Environmental Science and Engineering, University of Texas at El Paso, El Paso, TX, USA
[e] Department of Industrial Engineering, New Mexico State University, Las Cruces, NM, USA

ARTICLE INFO

Keywords:
Advanced oxidation process
Hydrogen evolution reaction
Metal organic framework
Porous carbon
Transition metal nanocatalysts

ABSTRACT

Synthesis of high-efficiency metal catalysts and their application in catalyzing critical chemical processes holds the key to the sustainable supply of water and energy. However, reaction-induced atomistic modifications of nanoclusters often result in reduced stability and efficacy. Herein, we report a highly active and multifunctional transition metal nanocatalysts encapsulated in porous carbon network (M@C where M = Cu, Ni, Fe, Co) prepared by leveraging the sacrificial templating properties of metal-organic frameworks (MOFs). The as-synthesized M@C nanocatalysts were employed for oxidative degradation of organic pollutants and electrocatalytic hydrogen generation. Fenton like catalytic studies revealed that the nanocatalysts were highly active and reusable following the order of Co@C > Fe@C > Cu@C > Ni@C. On the other hand, Ni@C electrocatalyst displayed superior activity towards hydrogen evolution reaction as compared to others, delivering a low onset potential of 61 mV, Tafel slope of 82 mV/dec and an overpotential of 286 mV at 10 $mA{\cdot}cm^{-2}$. The activity was essentially unchanged even after 500 cycles, suggesting the long-term stability under acidic conditions. The impressive multifunctional catalytic performances of M@C nanocatalysts are attributed to their unique porous carbon matrix doped by transition metal nanoparticles which provide a large number of interconnected catalytically active sites.

Introduction

Nowadays, the modern society demands for drinking water and clean energy sources are increasing rapidly due to the industrialization and fast population growth [1,2]. Heavy agro activities and industrialization are the primary sources of increased water contamination as a consequence of throwing harmful organic contaminants into the water ecosystems [3]. Among many water contaminants, the industrial dyes have been recognized as emerging organic pollutants that are extensively used not only in the printing, paint, tannery and textile industries but also widely used in agricultural research and food technology [4,5]. When they are discharged into the domestic water systems, they pose a serious threat on human health due to their non-biodegradability and toxicity characteristics [5]. As a result, they must be degraded or removed from wastewater to a satisfactory level before discharging into natural waters. As of now, different methods such as catalysis, adsorption and photocatalysis have been employed to remove organic dyes from wastewater [3,6,7]. Among them, the adsorbents are widely used to remove the organic dyes from wastewater. But the dye loaded sorbent materials still carry a possible risk to the ecological environment till they are removed using reactivation [3]. Among the reported methods, advanced oxidation processes (AOPs) including electrocatalytic oxidation, photocatalytic oxidation, ultrasonic treatment and ozonation are considered as easy, environmentally friendly and highly efficient

* Corresponding authors at: Department of Chemistry, University of Texas at El Paso, El Paso, TX, USA.
E-mail addresses: mahsan2@miners.utep.edu (M.A. Ahsan), sreenivasan@utep.edu (S. Sreenivasan), jcnoveron@utep.edu (J.C. Noveron).

https://doi.org/10.1016/j.mcat.2020.111241
Received 20 August 2020; Received in revised form 17 September 2020; Accepted 18 September 2020
Available online 16 October 2020

techniques to degrade organic compounds completely due to their ability of forming highly active radicals. The dye molecules can be oxidized and subsequently, mineralized to CO_2 and H_2O by the highly reactive radicals such as $^{\bullet}OOH$, $^{\bullet}OH$, O^{2-}, and $SO_4^{\bullet-}$ [8,9]. Among them, the sulfate radical has a longer life time (30–40 μs) and higher redox potential of 2.5–3.1 eV which makes them best candidate to decompose the toxic recalcitrant organic contaminants [10]. Peroxymonosulfate (PMS) is known to be a strong oxidizing agent that can generate sulfate radicals when activated by catalysts, UV irradiation, ultrasound or heating [10,11]. Though they can activate PMS to produce highly reactive radicals, but these methods are limited in practical applications because of their high energy input [11]. The alternative efficient way is to use transition metal nanoparticles for the activation of PMS. But the direct use of the metal nanoparticles in the bulk solution would certainly cause leaching of metal ions which is a critical bottle-neck [10]. Also, while considering the drawbacks of homogeneous process related to the loss of catalyst and the secondary pollution, it is therefore needed to develop novel metal based heterogeneous catalysts with a low cost, good stability, high activity and environmental benignancy.

Metal nanoparticles (MNPs) with superior electron dynamics, high surface area and excellent catalytic properties are intensely explored to develop novel technologies for energy and environmental applications [12,13]. However, MNPs (especially non-noble metal NPs) suffer from poor air stability as well as they tend to agglomerate owing to their high intrinsic surface energy and surface reactivity. Encapsulation of the MNPs in protecting shells can improve the air stability and decrease the agglomeration without significantly sacrificing catalytic performance [14]. Among different carbon-based and inorganic candidates; mesoporous carbon is an excellent protecting material due to their low density, excellent conductivity and stability [14,15]. While there are traditional multistep chemical techniques to synthesize supported nanocatalysts, they are generally expensive procedures and may involve the use of N_2 atmosphere, vacuum, high cost reducing agents and excessive evolution of gases [15,16]. Hence, significant research efforts are dedicated to formulate carbon encapsulated MNP catalysts through simple and cost-efficient pathways with negligible impact on the environment.

In this direction, recycling or repurposing existing materials and leveraging them as a precursor for encapsulated MNPs has gained increasing attention. The recycling of the materials especially through greener procedures without the use of any additional chemicals is especially advantageous because such procedure in addition to reducing the accumulation of the waste, will avoid the entry of new chemicals during synthesis [17,18]. Metal organic frameworks (MOFs) are a new class of crystalline and microporous inorganic–organic hybrid material with excellent potential as adsorbents, heterogeneous catalysts, gas storage system, as well as energy conversion and storage platforms [19,20]. The presence of organic linkers and metallic cations renders the MOF to be a perfect recycled precursor to prepare many carbon encapsulated metals and metal oxide-based systems [21,22]. While there are different MOFs, one drawback with MOFs is the requirement of expensive ligands, toxic organic solvents, high temperature and long synthesis time [14]. The goal of this work is to use an inexpensive and readily available ligand namely 1,4-benzene dicarboxylic acid (BDC) for making M-BDC MOFs (M = Cu, Ni, Fe and Co) MOFs so that they can used as a template for making M@C nanocatalysts.

The fabrication of renewable and environmentally friendly energy technologies including water splitting devices, fuel cells and even metal-air batteries are gaining a significant interest as promising alternatives towards the development of clean energy sources [23–25]. Electrochemical generation of hydrogen from water through the hydrogen evolution reaction (HER) is one of the most economical, sustainable and attractive methods for clean, secure and renewable energy source [26]. Currently, noble metal-based catalysts (e.g. Pt) are used as state-of-the-art catalysts to generate molecular hydrogen as well as to construct the efficient energy conversion devices [25,27]. However, their high cost and low natural abundance limits their wide applicability and their application to large-scale commercial purposes [26,27]. Recently, research related to the fabrication of inexpensive MNP-based alternate catalysts using MOFs as self-sacrificial templates is generating a lot of attention in the materials science community [28]. The capacity to transform 3D-MOFs into hierarchically nanostructured functional materials using green methodologies is opening new ways for the fabrication of green energy storage and conversion technologies. In this work, following a one-pot and simple carbonization process, we have synthesized four carbon encapsulated transition metal nanoparticles (Cu@C, Ni@C, Fe@C and Co@C) using MOFs as self-sacrificial templates. The morphology and composition of the as-synthesized M@C nanomaterials and their applicability as catalysts for both the degradation of organic pollutants through Fenton-like reaction and the electrochemical generation of molecular hydrogen were deeply explored. Hence, this contribution, through systematic variation of process parameters will engineer the structure, morphology and composition of the M@C nanocatalysts and study the correlation between the NP characteristics and its catalytic performance. By engineering the process parameters, we aim to unearth the ideal procedure to transform MOFs to M@C nanocatalysts with best catalytic performance and identify the type, morphology and composition of the best catalyst for specific processes.

Experimental

Materials

All of the reagents were of analytical grade and used as received. Peroxymonosulfate (PMS), peroxydisulfate (PDS), hydrogen peroxide, methylene blue (MB), methyl orange (MO), Congo red (CR), Cu $(NO_3)_2.2.5H_2O$, $Ni(NO_3)_2.6H_2O$, $Co(NO_3)_2.6H_2O$, $Fe(NO_3)_2.6H_2O$, benzene-1,4-dicarboxylic acid (BDC), 5,5-Dimethyl-1-pyrroline N-oxide (DMPO), Nafion solution (5 wt%) methanol (MeOH), tert-butanol, *N,N*-Dimethylformamide (DMF) and Pt/C (20 %) were purchased from Aldrich, Anachemia, Sigma Aldrich, Fisher Scientific and Sigma. Deionized (DI) water was obtained from the Milli-Q® instrument, Millipore Corporation.

Synthesis of M-BDC MOFs (M = Cu, Ni, Co and Fe)

Ni-BDC MOF was synthesized through a facile solvothermal technique by following a reported method with slight modification [29]. In a typical process, nickel nitrate (2160 mg) and BDC (396 mg) were dissolved separately in 30 mL of water and DMF. A stirring technique was employed to accelerate the dissolution. Then the two clear solutions were transferred into a glass vial. The mixture was then stirred for about 15 min. Finally, the glass vial was placed in an oven at 100 °C for 24 h. The sample was collected by vacuum filtration and washed with DMF and water for three times. The obtained green crystals were then dried in a vacuum oven at 70 °C for 12 h. Furthermore, Cu-BDC, Co-BDC and Fe-BDC MOFs were also prepared individually, following the above-mentioned procedures.

Synthesis of M@C (M = Cu, Ni, Co and Fe)

The Ni@C nanocomposite was synthesized through a green and facile carbonization treatment of the as-prepared Ni-BDC MOF. Briefly, the dried Ni-BDC MOF powders of about 500 mg were placed in a tubular furnace and heated to 600 °C for 1 h with a heating rate of 5 °C min^{-1} under Ar atmosphere and subsequently, cooled down to room temperature to get the Ni@C nanocatalyst sample. Cu@C, Co@C and Fe@C nanocomposites were also prepared by following the same method. The schematic diagram for the synthesis of Ni@C nanocatalyst is presented in Fig. 1**a**.

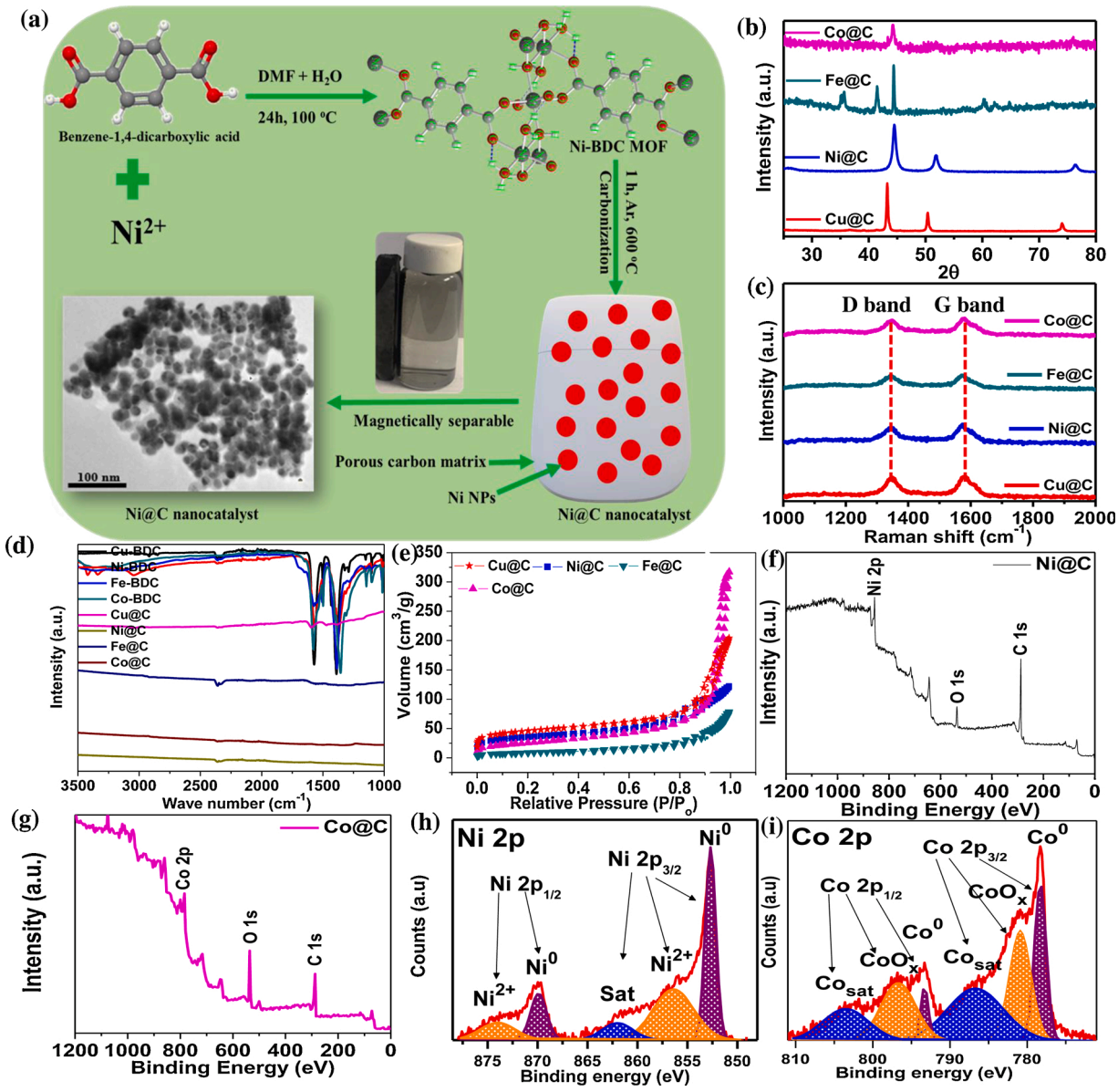

Fig. 1. (a) Synthesis scheme of Ni@C nanocatalyst; (b–e) XRD patterns, Raman spectra, FT-IR and N_2 adsorption-desorption isotherms of Cu@C, Ni@C, Fe@C and Co@C catalysts, respectively; (f–g) XPS survey spectra of Ni@C and Co@C catalysts, respectively; and (h–i) XPS spectra of Ni 2p and Co 2p levels of Ni@C and Co@C nanocatalysts, respectively.

Sample characterization

Bruker D8 Advance X-ray diffractometer was used to collect the X-ray diffraction or XRD patterns of the as-synthesized nanocomposite samples using the radiation of Cu Kα1 (λ =1.5406 Å). Fourier transform infrared spectroscopic (FT-IR) analysis of the prepared materials was performed on a Nicolet-6700 FTIR spectrometer. A scanning electron microscopy (SEM) equipped with an energy-dispersive X-ray spectroscopy (EDS) was used to collect the morphological images and EDS spectrum of the prepared samples [Model: Hitachi S-4800]. A Hitachi H-7650 transmission electron microscope (TEM) was used to obtain TEM images at nanoscale. Brunauer–Emmett–Teller surface area (BET) and pore volume measurements of the prepared nanocomposites were performed using a Micromeritics Surface Area and Porosity Analyzer (ASAP-2020). The electron paramagnetic resonance spectra were obtained using a Bruker ESR A-300 spectrometer having center field at 3516 G. XPS data were obtained using a Thermo Scientific Escalab 250Xi spectrometer. A monochromatic Al Ka (1486.68 eV) X-ray source was used to generate photoelectrons.

Catalytic activity tests

All the catalytic experiments were performed in a 50 mL glass vial with a constant stirring at 300 rpm at room temperature except for the temperature dependent study. The Cu@C, Ni@C and Co@C nanocatalysts prepared at 600 °C and the Fe@C nanocatalyst prepared at 800 °C were used in all of the catalytic experiments unless otherwise stated. At first, 10 mg of nanocatalysts were introduced into the glass vial having 40 mL of dye solutions with the chosen initial concentrations. Then the reaction mixture was bath sonicated for ten minutes to obtain a homogeneous mixture. Afterward, a specific amount of an oxidant (5 mM PMS /PDS /H_2O_2) was added to the reaction mixture to start the catalytic degradation reaction. To monitor the degradation process, 1 mL of dye solution were collected by a 0.45 μL syringe filter in every five minutes and quenched with 1 mL of pure methanol. All of the collected samples from the catalytic degradation experiments were then analyzed using a UV–Vis spectroscopy at an λ_{max} of 615 nm, 465 nm and 498 nm for MB, MO and CR, respectively. Furthermore, 5 mL of sample

was also taken out from the glass vial once the degradation process is complete for the ICP-OES analysis to monitor the concentration of the total dissolved metal ions. The temperature study was carried out using 40 mL of 50 ppm of MB solution and 10 mg of Co@C nanocatalyst at different temperature viz.25, 45 and 55 °C in an oil bath. The stability of the Co@C nanocatalyst was examined by recovering the used solid catalyst using an external magnet. The recycled sample was washed with water for several times, dried at 70 °C for 12 h and reused in the successive cycles. To identify the reactive species during the batch experiments, several radical scavengers were used to distinguish the hydroxyl and sulfate radicals. The dye degradation efficiency was calculated by using the following Eq. 1 [10].

$$\text{Degradation efficiency} = \frac{C_i - C_t}{C_i} \times 100(\%) \quad (1)$$

The catalytic degradation of MB was evaluated by using a pseudo-first order kinetic model and the model is expressed by Eq. 2 [10].

$$\ln (C_t/C_i) = -Kt \quad (2)$$

Where t is time, K is the rate constant, C_i and C_t are the concentrations at time 0 and t, respectively.

Electrochemical measurement

HER experiments were conducted using an electrochemical workstation (CHI 660D). The set up was consisted of three-electrode system. Glassy carbon, graphite rod and Ag/AgCl (in 3 M KCl solution) electrodes were used as a working, counter and reference electrode, respectively. In a typical experiment, 4 mg of nanocatalysts and 30 μL of Nafion solution were dispersed in 1 mL of ethanol by bath sonicating for 30 min to obtain a homogeneous ink. Then 10 μL of the catalyst ink was drop casted onto the working electrode with a diameter of 3 mm. A reversible hydrogen electrode (RHE) was used to calibrate all of the potentials. The working electrode was always polished before each experiment with Al_2O_3 powders (size 0.05 μm). Linear sweep voltammetry (LSV) was performed at a scan rate of 2 mV·s^{-1} in 0.5 M sulfuric acid aqueous solution for HER process. Electrochemical impedance spectroscopy (EIS) analysis was performed at −0.3 V vs RHE for the HER reaction in a wide range of frequency of about 0.01 – 10^5 Hz. The Tafel equation, as given in Eq. 3 was used to obtain the Tafel slopes [30].

$$\eta = a + b^* \log (j) \quad (3)$$

Where b is the Tafel slope (mV·dec^{-1}), j is the current density (mA·cm^{-2}) and η is the applied overpotential (mV).

Cyclic voltammetry techniques were employed at different scan rates (5, 10, 20, 50, 100 and 200 mV·s^{-1}) in a narrow potential window (0.1-0.3 V vs RHE) where there are no faradaic contributions to obtain the electrochemically active surface area (ECSA) of the M@C catalysts. A linear relationship was achieved by plotting J_{anodic}-$J_{cathodic}$ (at 0.15 V vs RHE) vs scan rate to estimate the double layer capacitance (C_{dl}) and then the ECSA was estimated using the following equation [30].

$$\text{ECSA} = \frac{C_{dl}}{C_s} \quad (4)$$

where C_s is specific capacitance and the C_s value is reported to be 0.035 mF·cm^{-2} in acidic media for transition metal-based electrocatalysts [7].

The roughness factor (RF) was estimated using the following equation 5 [30].

$$\text{RF= (ECSA) / (geometric area of the electrode)} \quad (5)$$

Results and discussion

Characterization of the M@C nanocatalysts

The transition metal-based MOFs namely Cu-BDC, Ni-BDC, Fe-BDC and Co-BDC MOFs were synthesized in this study using a facile and green solvothermal method by simply mixing the corresponding metal salts with the 1,4-benzene dicarboxylic acid (BDC) ligand. These synthesized MOFs were used as parent materials for making porous carbon encapsulated transition metal nanoparticles (Cu@C, Ni@C, Fe@C and Co@C) by employing carbonization method. The as-synthesized materials were thoroughly characterized using XRD, Raman, TGA, FT-IR, SEM, TEM, EDS and BET instruments [31,32].

The crystal structure as well as the phase composition of M@C nanocatalysts were studied using XRD and the collected patterns are shown in Fig. 1**b**. As seen, XRD analysis of the Cu@C nanocatalyst showed three prominent peaks at 43.6, 50.8 and 74.4°, which corresponds to the crystal plane of (111), (200) and (220), respectively. It was found that the diffraction patterns correspond to JCPDS No. 04-0836 indicating that the structure of the synthesized Cu nanoparticles were face centered cubic [33]. The XRD pattern of the Ni@C nanocatalyst showed three distinct peaks at 44.48, 51.28, and 76.35° which corresponds to miller indices of (111), (200) and (220), respectively. The obtained diffraction patterns of the Ni@C sample are well matched with JCPDS No. 04-0850 confirming their face centered cubic structure [14]. The Fe-BDC MOF was carbonized at three different temperatures viz. 600, 700 and 800 °C to make Fe@C nanocatalyst. Unfortunately, the carbonation temperature 600 and 700 °C were not enough to make Fe@C nanocatalyst from the MOF rather it made iron oxide as confirmed by the XRD analysis and the results are shown in **Fig. S1**. As seen in Fig. 1**b** for Fe@C sample prepared at 800 °C, the XRD diffraction peaks centered at 44.8°, 65.1°, and 82.4° could be attributed to the body centered cubic phase of pure metallic Fe [34]. Also, there are still some peaks of Fe_3O_4 along with the metallic iron at around 30°, 35°, 43°, 57° and 63°, demonstrating that the carbonization process could not able to achieve the complete phase transformation. Furthermore, this might also happen because of the oxidation of the Fe NPs during the exposure or handling of the Fe@C nanocatalyst to air. A similar result has been reported earlier [35]. The Co@C nanocatalyst sample also exhibited three sharp diffraction peaks at around 44.2, 51.5 and 75.9° (JCPDS no. 15-0806) that correspond to the crystal planes of (111), (200) and (220), respectively indicating the face centered cubic structure of the prepared Co@C. These XRD results confirmed the successful synthesis of M@C nanocatalysts [36]. Raman spectroscopic analysis of the prepared M@C nanocatalysts was further carried out to investigate the degree of graphitization and the results are presented in Fig. 1**c**. As seen, all of the M@C samples showed two broad bands at around 1340 cm^{-1} and 1570 cm^{-1} that correspond to D and G band, respectively [37]. These G and D bands provide important information on the crystallinity and disorder of the sp^2 type carbon materials, respectively [37]. As seen in Fig., the intensity ratios (I_D/I_G) of the D to G band were found to be 0.88, 0.82, 0.94 and 0.87 for the Cu@C, Ni@C, Fe@C and Co@C nanocatalysts, respectively indicating the degree of crystallization of the graphitic or sp^2 type carbon. These obtained I_D/I_G values for all of the samples were comparable to the measured I_D/I_G values of GO and rGO (~1), showing the formation of 3D graphitic type carbon [38].

FTIR experiments were performed to examine the chemical structure as well as to find the corresponding functional groups of the parent MOFs along with those MOF derived M@C nanocatalysts, as presented in Fig. 1**d**. As seen, two sharp and broad characteristic IR peaks were observed in all of the prepared MOF samples namely Cu-BDC, Ni-BDC, Fe-BDC and Co-BDC MOFs.

The first one was observed at ~ 1398 cm^{-1} for the symmetric vibrational modes of the carboxyl groups in BDC organic linker and likewise, the second one was observed at ~ 1597 cm^{-1} for the asymmetric vibrational modes of the same functional group in the BDC linker,

indicating the presence of BDC linker in the prepared MOF samples [39]. The MOF samples were carbonized at higher temperatures to make M@C nanocomposites and the organic part of the MOFs were expected to be decomposed after the carbonization treatment. This was verified by the FT-IR analysis of the prepared M@C nanocatalyst samples. It is obvious from the figure that all of the characteristic peaks correspond to the MOFs are disappeared in the corresponding M@C nanocatalyst samples as the organic linkers are decomposed at higher temperature.

In order to understand the mesostructure of the M@C nanocatalysts, N_2 adsorption and desorption measurements were performed. The corresponding results are presented in Fig. 1**e** and **Table S1**. Based on the BET results, the surface area per gram of these nanocatalysts from smallest to largest is Fe@C (30.77 $m^2\ g^{-1}$) < Ni@C (92.27 $m^2\ g^{-1}$) < Cu@C (120.32 $m^2\ g^{-1}$) < Co@C (153.85 $m^2\ g^{-1}$). BJH average pore sizes were also calculated based on the average of adsorption and desorption pore size values, with average pore diameter from smallest to largest being Cu@C (9.39 nm) < Co@C (13.98 nm) < Fe@C (15.51 nm) < Ni@C (23.41 nm) (**Table S1**). The smaller pore sizes of Cu@C and Co@C correlate with the overall larger specific surface area of these two heterogeneous catalysts relative to Fe@C and Ni@C. Surface analysis of Ni@C and Co@C nanocatalysts was further carried out using X-ray photoelectron spectroscopy (XPS) measurements. The XPS survey spectrum (Fig. 1**f** and g) evidences the coexistence of C, O and Ni elements in Ni@C sample and C, O and Co elements in Co@C sample, respectively. A high-resolution Ni (2p) and Co (2p) spectrum were further recorded to investigate the chemical states of the Ni and Co active components (Fig. 1**h** and i). The $2p_{1/2}$ and $2p_{3/2}$ core levels of the carbon encapsulated metallic nanoparticles were deconvoluted to elucidate the oxidation states of the metallic nanostructures. The obtained results demonstrated that both of the samples have pure metallic state (0) along with oxide state (+2) [40,41]. The exposure of Ni and Co NPs to air could make a thin NiO/CoO shell since the NPs are sensitive to the aerobic atmosphere. But, the dominant existence of Ni(0) and Co(0) in the XPS measurements indicated that the metallic nanoparticles are mainly present in the samples.

SEM analysis was carried out to determine the morphological structures of the parent MOFs as well as their derived M@C nanocomposites and the results are presented in **Fig. S2**. SEM analysis revealed that the morphologies are looks like needle, cuboid, rectangular and shale-shaped for the Cu-BDC, Ni-BDC, Fe-BDC and Co-BDC MOFs, respectively (**Fig. S2(a, c, e and g)**). It was also found that the MOFs particles are micron in size. But after the carbonization, the SEM images of the MOF derived M@C nanocatalysts showed that the nanosized Cu, Ni, Fe and Co particles covered their respective MOF surfaces as seen in **Fig. S2 (b, d, f and h)**, respectively and those particles are highly dispersible all over the surfaces. It can be summarized form the SEM images of the M@C nanocatalysts that the parent MOF materials showed their highly stable nature for being a support or self-sacrificial template to prepare transition metal NPs due to the fact that a little change has been observed on their morphology though the MOF surfaces are little distorted after the carbonization process. EDS analysis was carried out for the elemental analysis of the prepared M@C nanocomposites and the results are presented in **Fig. S3**. As seen in **Fig. S3**, the EDS analysis of Cu@C nanocatalyst showed different peaks corresponding to carbon and copper. It was also found that the EDS peak of copper is very intense as compared to the carbon peak indicating that the Cu@C nanocomposite consists of mostly copper metal. Likewise, the Ni@C, Fe@C and Co@C nanocatalyst samples showed very similar result having higher quantity of nickel, iron and cobalt, respectively.

The strong Cu, Ni, Fe and Co peaks demonstrate that the nanocomposite samples are highly metallic in nature. TEM and HR-TEM analysis were further performed to get in depth information about the morphology and crystalline structure of the as-synthesized M@C nanocatalysts and the results are illustrated in Fig. 2**(a–d)**. As seen, the Cu, Ni, Fe and Co nanoparticles are well dispersed and deposited on the surface of the MOF derived porous carbon matrix. All of the NPs are well distributed all over the carbon matrix as well as encapsulated by the porous carbon. This porous carbon wrapping helps them to be stable even in presence of air and protects them from further oxidation. It was also found that some kind of agglomeration is happened in the Fe@C

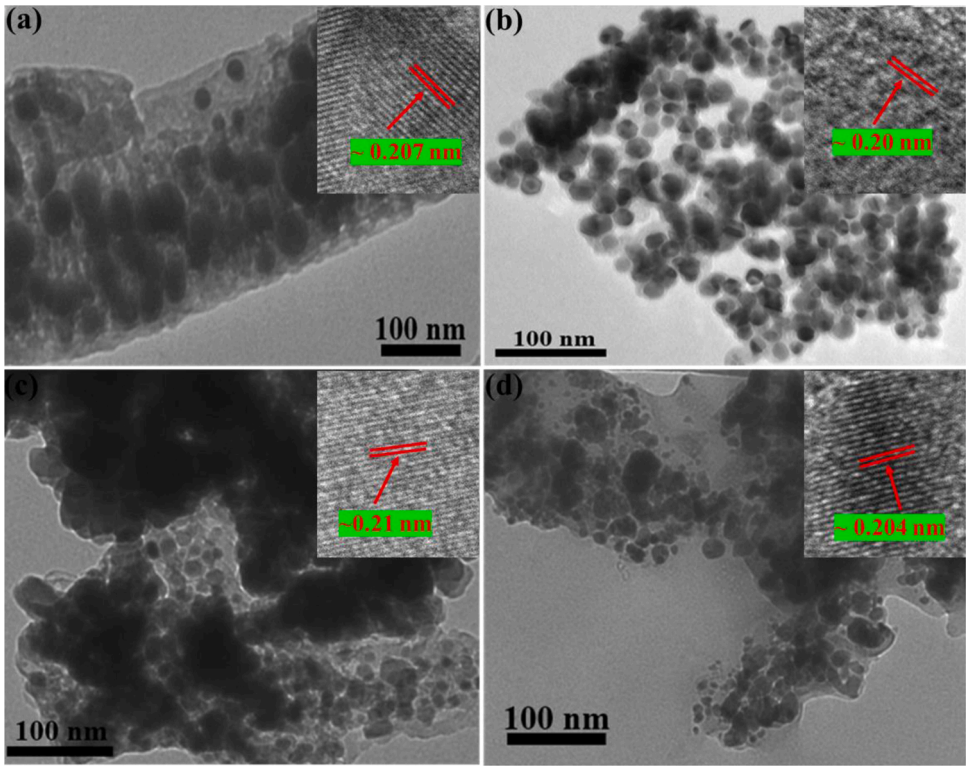

Fig. 2. (a–d) TEM images of Cu@C, Ni@C, Fe@C and Co@C nanocatalysts, respectively [inset: HRTEM images of the corresponding nanocatalysts].

sample. This is due to the preparation of Fe@C sample at higher carbonization temperature (800 °C), as the higher temperature favors faster nucleation which let the particles agglomerate easily. As seen from the HR-TEM images of M@C nanocatalysts in Fig. 2**(a-d: inset)**, the calculated atomic lattice fringes are of about ~0.207, 0.20, 0.21 and 0.204 nm approximately for the Cu, Ni, Fe and Co NPs, respectively corresponding to the Cu (111), Ni (111), Fe (110) and Co (111) lattice planes. These results confirmed that the nanoparticles are highly crystalline in nature [40–42].

Evaluation of the catalytic performance of M@C catalysts for oxidative degradation of MB via peroxymonosulfate

To investigate the catalytic performance of the prepared M@C nanocatalysts, the effect of various oxidants such as PMS, PDS and H_2O_2 on the degradation of methylene blue as a model organic pollutant was carried out and the results are shown in Fig. 3**(a–c)**. While the MB was not degraded by either the nanocatalysts or oxidants alone, MB was significantly removed when the oxidant and M@C nanocatalysts were used together, demonstrating that M@C nanocatalysts coupled with oxidants is an efficient method for the decontamination of the organic contaminants. In case of PMS oxidant, the catalytic performance is followed by the order of Co@C > Fe@C > Cu@C > Ni@C as shown in Fig. 3**a**. The removal percentages of MB were 96.86 % for Co@C, 83.72 % for Fe@C, 72.95 % for Cu@C and 62.7 % for Ni@C in 30 min, respectively. The reaction rate constants were also calculated for the above-mentioned MB degradation reactions by M@C/PMS system and the results are shown in **Fig. S4a**. The Co@C nanocatalyst mediated MB degradation reaction showed highest rate constant (0.0524 min^{-1}) as seen in the figure. XRD, TEM, Raman and BET analysis show that all of the M@C nanocomposites have the similar degree of carbon crystallinity and structural features, thus the observed difference in PMS activity for MB degradation can only be attributed to the different metal core compositions. Also, the results clearly demonstrate that the presence of metals in the M@C structure strongly influenced the MB degradation, indicating that there might be a synergistic effect between the C and M species in the M@C nanocatalyst system. BET and BJH measurements taken together indicate that the Co@C and Cu@C have both substantially higher surface area and smaller pores, which indicates a more uniform mesostructure. Given the similarity of mesostructure between Co@C and Cu@C, the relatively better catalytic performance of Co@C seems to be primarily due to the nature of Co NP's vs. Cu NP's as catalytic particles. Both Fe@C and Ni@C have larger pore sizes and lower total surface area on average than the other catalysts. While larger pore sizes may allow easier diffusion of solutes, the relatively lower surface area may mean fewer interfaces at which reactions can occur.

Afterward, the PDS was employed as an oxidant along with the nanocatalysts for the degradation of MB dye and the results are shown in Fig. 3**b**. It is clear from the figure that the incorporation of the PDS also caused dye degradation but was slow than the PMS. The observed activity was found to be in the order of Ni@C < Cu@C < Fe@C < Co@C and the degradation efficiencies were found to be 31.86, 26.50, 43.67 and 55.06 % for the Cu@C, Ni@C, Fe@C and Co@C nanocatalysts, respectively. In addition, the Co@C nanocatalyst also showed highest

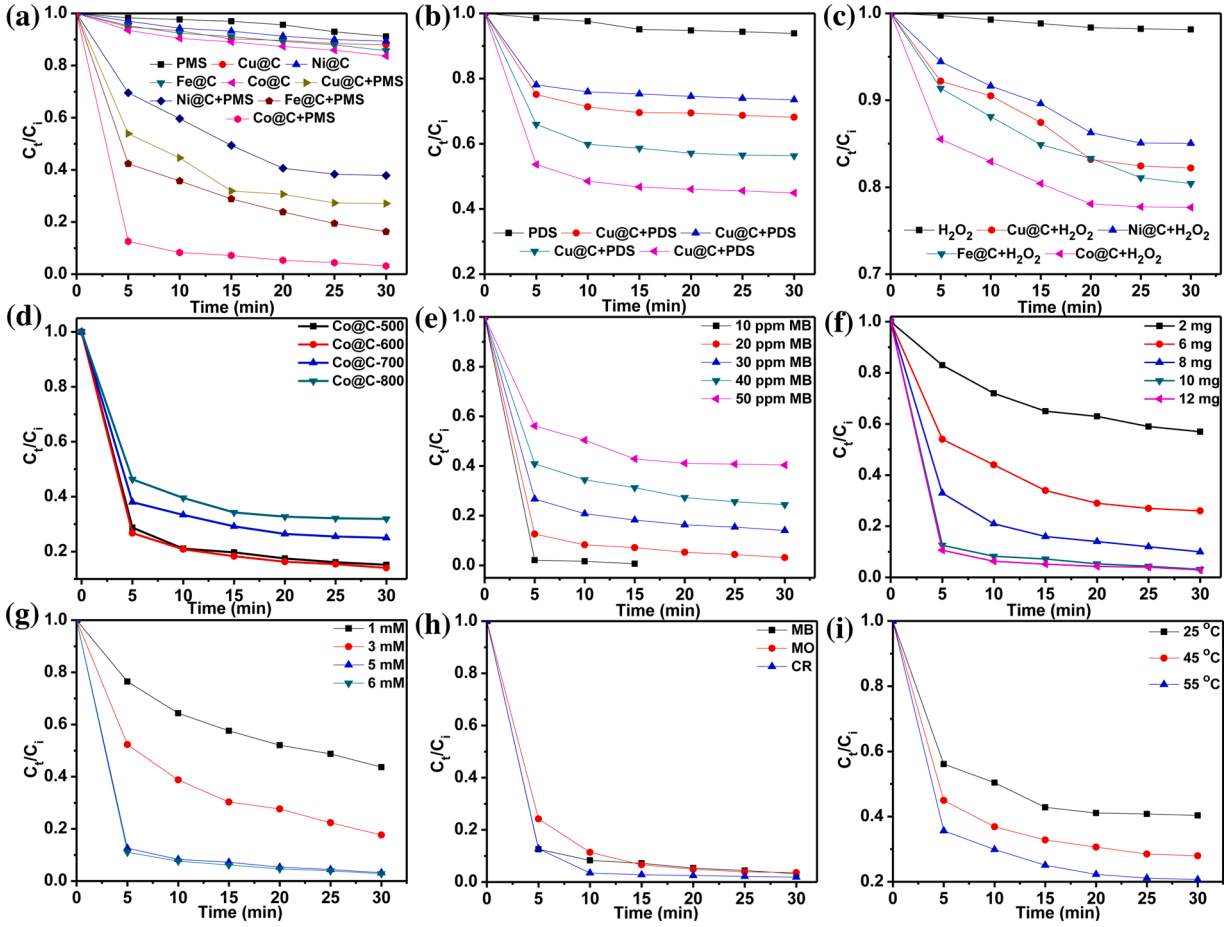

Fig. 3. (a–c) Catalytic performance of the prepared nanocatalysts for MB degradation in presence of different oxidants such as PMS, PDS and H_2O_2, respectively; the effect of different parameters on the degradation of organic pollutants by Co@C nanocatalyst: (d) different carbonization temperature, (e) different MB initial concentration, (f) catalyst dosage, (g) different PMS concentration, (h) different dyes and (c) reaction temperature. Unless otherwise stated, conditions: [dye]= 20 ppm; [nanocatalyst]=10 mg; [PMS]=5 mM and [Temperature]=25 °C.

rate constant of about 0.0062 min^{-1} as seen in **Fig. S4b**. Furthermore, H_2O_2 oxidant was also used for the MB degradation and the results are illustrated in Fig. 3**c**. The observed degradation performance was very slow for all the nanocatalysts because of the low oxidizing character of H_2O_2. The calculated degradation efficiencies were only about 17.78, 14.96, 19.57 and 22.33 % for the as prepared Cu@C, Ni@C, Fe@C and Co@C nanocatalysts, respectively. Therefore, it is clear from these experiments that the PMS is the best oxidant and Co@C is the best nanocatalyst than the other three transition metals to activate PMS [43]. The unsymmetrical nature of PMS seemed to make it more activated than H_2O_2 and PDS which have symmetrical structures [44]. The obtained results in this study are comparable with the previously reported homogeneous as well as heterogeneous catalytic oxidation, in which the PMS exhibited a significant reactivity [45,46].

In these studied catalytic systems, the total dissolved cobalt ion concentration was detectable but the detected concentration was very low that is close to the experimental error. This result indicates that the released ions are not dominant in the catalytic degradation of MB. It can be summarized that the activation of PMS by M@C is mainly heterogeneous type that is happening on the catalyst surface. The Fenton like oxidative degradation of MB by Co@C/PMS system was monitored using a UV–vis spectroscopy and the corresponding results are shown in **Fig. S5**. It is obvious from the figure that the adsorption bands of MB at 615 nm and 660 nm start to diminish with time after the incorporation of Co@C nanocatalyst and PMS in MB dye solution and this happens as a result of the fragmentation of the N═N bonds in MB dye -by the Co@C/PMS system. The difference in absorption spectrum of the MB dye is consistent with a clear color change of the MB solution with increasing time.

To investigate the process parameter such as carbonization temperature on the overall catalytic performance of the Co@C nanocatalyst, we have also prepared the Co@C nanocatalyst at different carbonization temperatures viz. 500, 700 and 800 °C along with 600 °C and used them for the oxidative degradation of 30 ppm of MB solution in presence of PMS. The results are presented in Fig. 3**d**. As seen, the catalytic performance of the Co@C nanocatalyst decreases with increasing the carbonization temperature. To understand this fact, we have conducted the XRD and TEM analysis of the nanocatalysts and the results are given in **Fig. S6** and **Fig. S7 (a–c)**. XRD analysis confirm the successful synthesis of the metallic cobalt in all samples, whereas, the TEM analysis shows that the size of the cobalt nanoparticles increases with increasing carbonization temperature.

At higher temperature, the nucleation of the particles happens faster resulting higher aggregation of the particles which in turn decreases the surface are as well as decreases the number of active sites. This could be the reason for lower catalytic performance of the Co@C nanocatalysts prepared at higher carbonization temperatures.

The effect of initial MB concentration on its degradation efficiency was studied and the results are shown in Fig. 3**e**. As seen in the figure, the removal efficiency of MB decreased from 96.86 % to 59.62 % while increasing the initial concentration of MB from 10 ppm to 50 ppm. Also, it took only 15 min to degrade 99.36 % of 10 ppm MB, while it degraded only 59.62 % of 50 ppm MB in 30 min. Therefore, the removal of higher MB initial concentration seems to require more PMS that may cause secondary pollution due to the release of excess sulfate. The degradation efficiency of MB with different amount of Co@C nanocatalysts were also carried out and the results are shown in Fig. 3**f**. In a catalyst/PMS system, the catalyst always plays a vital role due to the synergistic effect between the PMS and catalyst. More reactive sites can be achieved by increasing the amount of catalysts, therefore producing more active radicals [11,47]. As seen from the figure, the degradation efficiency of MB increased from 43.1%–96.86 % in 30 min as the amount of Co@C catalyst increased from 2 mg to 10 mg, indicating that the increased catalyst amount provided more reactive catalytic sites. Thus, this method is a good way to increase the degradation efficiency of MB. But, the removal efficiency of MB enhanced slightly from 96.86%–98.71 %, while further increasing of the catalyst dosage from 10 mg to 12 mg and this could be due to the limited PMS concentration. Therefore, the optimal amount of catalyst was 10 mg in this study.

The removal efficiency of MB with different PMS concentrations were also studied and the results are shown in Fig. 3**g**. As seen in the figure, the removal of MB was increased as the PMS concentration increased. The removal efficiency of MB was increased from 56.36%–96.86 %, when the PMS concentration was increased from 1 mM to 5 mM. Further increase of PMS concentration did not improve the removal efficiency significantly. The available active sites of the catalyst could not be efficiently utilized at lower PMS concentration. At this stage, PMS is the limiting factor. But, as the PMS concentration increased, the usage of reactive sites on the catalyst surface was gradually saturated. Then again, addition of excessive PMS might lead to the self-quenching of sulfate and hydroxyl radicals [48,49]. As a result of the quenching of the active radicals, weaker peroxymonosulfate radicals ($SO_5^{\bullet -}$) or hydroperoxyl ($HO_2^{\bullet}$) are generated or self-reactions between the sulfate radicals might happen which leads to form $S_2O_8^{2-}$ before the degradation of MB. The corresponding reactions are explained by the following Eq.s (6–10) [48,49]. Based on the obtained results, 5 mM PMS was used in the catalytic degradation reactions.

$$HSO_5 + SO_4^{\bullet -} \rightarrow SO_4^{2-} + SO_5^{\bullet -} + H^+ \quad (6)$$

$$HSO_5 + {}^{\bullet}OH \rightarrow SO_5^{\bullet -} + H_2O\ CO_2 \quad (7)$$

$$HSO_5 + SO_4^{\bullet -} + H_2O \rightarrow 2SO_4^{2-} + HO_2{}^{\bullet} + H^+ \quad (8)$$

$$HSO_5 + {}^{\bullet}OH \rightarrow SO_4^{2-} + HO_2{}^{\bullet} + H^+ \quad (9)$$

$$SO_4^{\bullet -} + SO_4^{\bullet -} \rightarrow S_2O_8^{2-} \quad (10)$$

Furthermore, several organic pollutants such as methylene blue, methyl orange and congo red were efficiently degraded by the Co@C/PMS system at more than 96.86 %, 96.38 % and 98.14 % removal efficiencies in 30 min, respectively as seen in Fig. 3**h**. The degradation rates varying from each other might be ascribed to the difference in pollutants molecular structures. Overall, these findings confirmed that the Co@C/PMS system can be used effectively for the catalytic oxidation of numerous organic contaminants. We also carried out the temperature dependent study on the removal efficiency of MB at three different temperatures and the corresponding results are illustrated in Fig. 3**i**. It is cleared from the figure that the catalytic performance of the Co@C nanocomposite increased sharply at the elevated temperatures. The degradation efficiencies of MB at 25, 45, and 55 °C were found to be 59.62 %, 72.03 % and 79.31 %, respectively, indicating that the temperature has a great effect on the catalytic activity. This is due to the formation of more active radicals during the thermal activation of the PMS oxidant in aqueous solution [48]. Besides, the MB molecules can easily overcome the activation energy of the reaction at higher temperatures.

The recyclability and stability of the prepared Co@C which is most active nanocatalyst in this work was examined by successive tests of MB degradation using the same reaction conditions and the results are shown in Fig. 4**a**. When the freshly prepared Co@C nanocatalyst was used for the MB degradation, 96.86 % of MB was degraded within 30 min of reaction time. After each cycle, the used catalyst was separated by using an external magnet and washed with DI water for several times. Then the washed samples were vacuum oven dried at 60 °C for 12 h and used for the next cycle. As seen in the figure Fig. 4a, the catalytic performance of the Co@C nanocatalyst decreased slightly and after fourth cycle, the removal efficiency of MB decreased from 96.86%–88.76 %. As seen in Fig. 4c, it was found that the rate constant of the MB degradation reactions also decreased slightly while increasing the usage of the nanocatalyst and this happens because of the coverage of the formed intermediates during the MB degradation reactions on the reactive sites of the Co@C surface. These results recommended that the prepared Co@C nanocatalyst is an efficient and stable heterogeneous

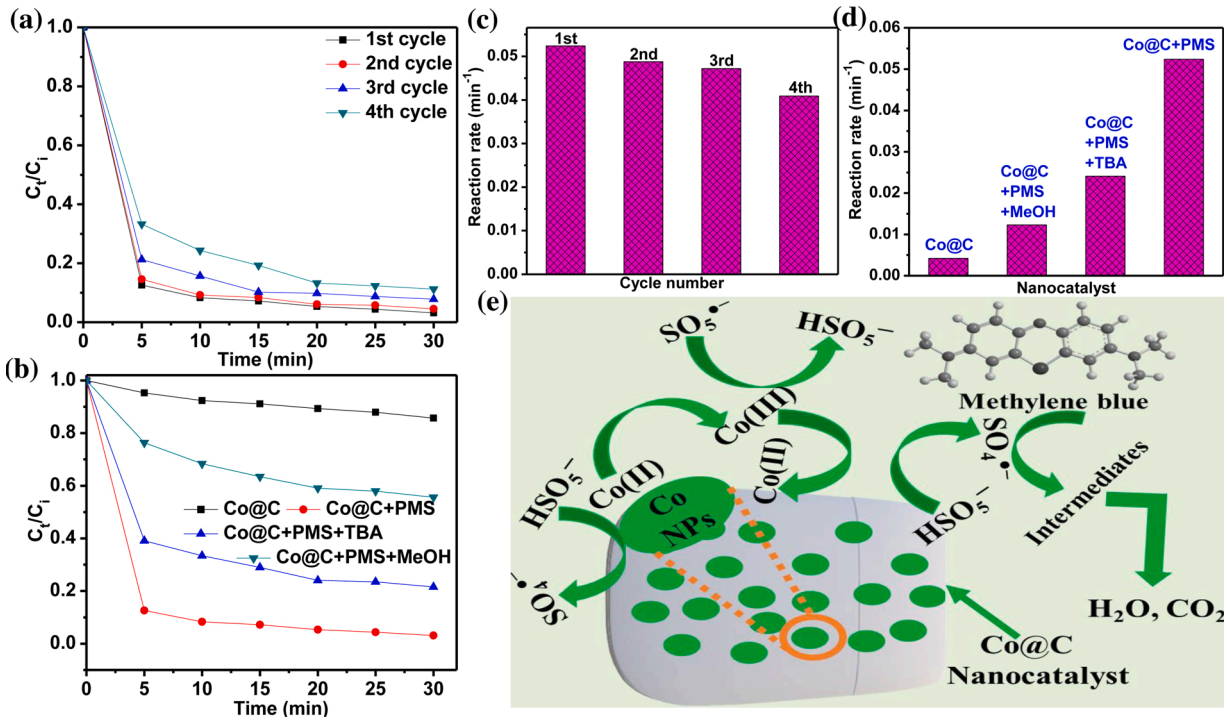

Fig. 4. (a) Cyclic stability of Co@C nanocatalyst for the degradation of MB; (b) effect of different radical scavengers on MB degradation; (c) the observed reaction rate constants for (a); (d) the observed reaction rate constants for (b) and (e) the proposed degradation mechanism of MB via PMS activation on Co@C nanocatalyst. Unless otherwise stated, conditions: [dye]=20 ppm; [nanocatalyst]=10 mg; [PMS]=5 mM and [Temperature]=25 °C.

catalyst for Fenton-like reactions.

Quenching experiments were performed in order to identify the contribution of free radicals toward the catalytic degradation of MB, as well as to know the underlying reaction mechanisms. Sulfate and hydroxyl radicals are usually considered as the main radical species that are generated from the decomposition of PMS mediated by the catalysts. It is well known that the methanol (MeOH) has the capacity to quench both $^{\bullet}OH$ and $SO_4^{\bullet-}$ with rate constants of 9.7×10^8 and 3.2×10^6 $M^{-1}s^{-1}$, respectively because of its higher reactivity [50]. Additionally, tert-butanol (TBA) is mostly utilized to quench only $^{\bullet}OH$, due to its faster rate constant with $^{\bullet}OH$ [$(3.8–7.6) \times 10^8$ $M^{-1}s^{-1}$] than with $SO_4^{\bullet-}$ [$(4–9.1) \times 10^5$ $M^{-1}s^{-1}$] [51]. The catalytic degradation of MB in the presence of methanol and tert-butanol can be seen in Fig. 4**b**. As seen, the adsorption equilibrium of MB using the Co@C nanocatalyst were reached in 25 min and the removal of MB was less than 15 % through adsorption. In the Co@C/PMS system, 96.86 % of MB was removed without the addition of MeOH or TBA. But when the TBA was added in the Co@C/PMS system for the MB degradation, the removal efficiency of MB decreased from 96.86 % to 78.47 %, indicating that the influence of hydroxyl radical in the degradation of MB was limited. On the other hand, the removal efficiency of MB decreased from 96.86 % to 44.36 % after the addition of MeOH to the Co@C/PMS system. These findings suggested that the sulfate radical played a vital role in the MB degradation process. Similar results also found in case of obtained reaction rate constants as seen in Fig. 4**d**. According to the above-mentioned findings and the previously reported literatures [50–52], a possible reaction mechanism is proposed for the Co@C/PMS system. In this present study, zerovalent cobalt was utilized as an alternative source of Co (II) for the oxidative degradation of MB by activating PMS. Co (II) can be released via zerovalent cobalt corrosion. under the aerobic conditions. In the process, the released OH^- ions upon the oxidation of zerovalent cobalt could neutralize the generated H^+ ions during the PMS decomposition [50]. Also, the PMS could directly react with the zerovalent cobalt to release Co (II) [50]. Afterwards, HSO_5^- is activated by the Co (II) to produce sulfate radicals ($SO_4^{\bullet-}$), however HSO_5^- can also be activated by Co (III) to produce $SO_5^{\bullet-}$. It is well known that the oxidation capacity of $SO_5^{\bullet-}$ is much lower than $SO_4^{\bullet-}$. Therefore, the degradation of MB was mainly because of the contribution of $SO_4^{\bullet-}$. Moreover, the sulfate radicals could react with H_2O to generate $^{\bullet}OH$. The corresponding reactions are presented in Eq. (11–17) [50–53]. The proposed mechanism of the MB degradation by PMS/Co@C system is shown in Fig. 4**e**.

$$Co\ (0) \rightarrow Co\ (II) + 2e^- \quad (11)$$

$$Co\ (0) + O_2 + 2H_2O \rightarrow Co\ (II) + 4\ OH \quad (12)$$

$$Co\ (0) + 2HSO_5 \rightarrow Co\ (II) + 2SO_4^{\bullet-} + 2OH \quad (13)$$

$$HSO_5 + Co\ (II) \rightarrow Co\ (III) + SO_4^{\bullet-} + OH \quad (14)$$

$$HSO_5 + Co\ (III) \rightarrow Co\ (II) + SO_5^{\bullet-} + H^+ \quad (15)$$

$$SO_4^{\bullet-} + H_2O \rightarrow SO_4^{2-} + H^+ + {}^{\bullet}OH \quad (16)$$

$$SO_4^{\bullet-} / {}^{\bullet}OH + MB \rightarrow Intermediates \rightarrow CO_2 + H_2O \quad (17)$$

Electrocatalytic performances of the MOF derived M@C nanocatalysts

In recent years, MOF-derived transition metal nanoparticles have sparked a lot of attention as highly efficient energy-related materials due to the desirable properties for electrocatalysis of the resulting hierarchical porous carbon matrix as well as its synergistic interaction with the metal cores [54–56]. The as-synthesized carbon encapsulated transition metal nanoparticles were tested for the electrochemical production of molecular hydrogen. The HER activity was evaluated under acidic conditions (0.5 M H_2SO_4) using linear sweep voltammetry (LSV) measurements as shown in Fig. 5**a**. The obtained onset potential values were found to be – 0.061 V, -0.540 V, -0.570 V and -0.635 V for Ni@C, Co@C, Fe@C and Cu@C nanocatalysts, respectively (**Table S2**). As shown in Fig. 5**a**, Ni@C nanocatalyst substantially surpassed the HER

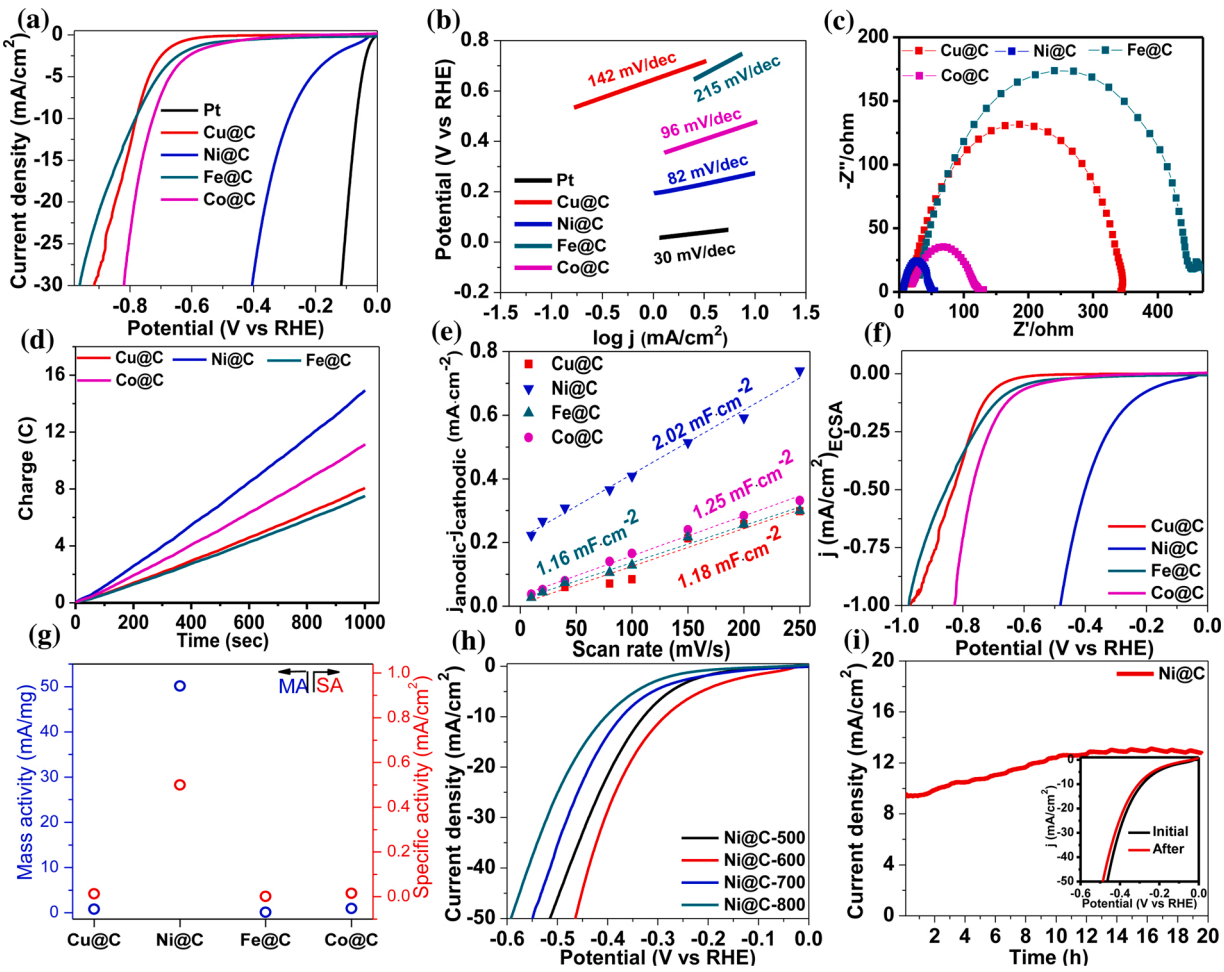

Fig. 5. (a) HER polarization curves; (b) Tafel plots; (c) Nyquist plots of the as prepared nanocatalysts; (d) Chronocoulometric measurements of M@C nanocatalysts; (e) plots of difference of anodic and cathodic current densities vs scan rate for the MOF-derived metal nanoparticles; (f) LSV polarization curves normalized by ECSA for Cu@C, Ni@C, Fe@C and Co@C; (g) Mass activity (MA) and specific activity (SA) values for all nanocatalysts; (h) LSV polarization curves of HER by the Ni@C nanocatalysts prepared at different carbonization temperatures at a scan rate of 2 mV/s in 0.5 M H_2SO_4 solution and (i) chronoamperometric measurements of the Ni@C nanocatalyst within 20 h at 0.5 V (inset: HER polarization curves of the Ni@C nanocatalyst initially and after 500 cycles).

performances of other nanoparticles delivering a low onset potential of -0.061 V vs. RHE and an overpotential of 286 mV vs. RHE at a current density of 10 mA·cm^{-2}, which is comparable or even better than those of the recently reported transition metal-based electrocatalysts (**Table S3**). The high electrocatalytic activity of Ni@C was also demonstrated by comparing the Tafel plots of the as-synthesized nanoparticles (Fig. 5b**).** A Tafel slope of 82 mV/dec was observed for Ni@C nanoparticles while the Tafel slopes of other nanocatalysts (Co@C, Cu@C and Fe@C) vary from 96 to 215 mV/dec, suggesting that Ni@C followed the most efficient electrocatalytic HER kinetic pathways, leading to a Volmer−Heyrovsky mechanism, in which the desorption of hydrogen is the rate limiting step. Importantly, the proposed HER mechanism in acidic media can be explained by three possible reaction steps [57,58]. The first Volmer step is electrochemical hydrogen adsorption:

$$H_3O^+ + e^- + M \rightarrow MH_{ads} + H_2O \quad (18)$$

This is followed either by Heyrovsky step (electrochemical desorption)

$$MH_{ads} + e^- + H^+ \rightarrow M + H_2 \quad (19)$$

or Tafel step (chemical desorption)

$$2MH_{ads} \rightarrow 2M + H_2 \quad (20)$$

Where M donates an empty metal active site and MH_{ads} represents an adsorbed H intermediate.

To further illustrate the superior HER performance of Ni@C nanoparticles, we have conducted electrochemical impedance spectroscopy (EIS) measurements of the MOF-derived carbon encapsulated nanoparticles (Fig. 5c). The observed semicircle at higher frequency corresponds to the charge transfer resistance (R_{ct}) between the electrocatalyst/electrolyte interfaces which in turn is associated with HER kinetics [59–61]. The charge transfer resistance (R_{ct}) is mainly determined by the diameter of the half circle, and it is evident that the R_{ct} value for Ni@C is much smaller compared to the another MOF derived metal nanoparticles indicating that the ions transport at the Ni@C catalytic surfaces is by far the fastest ET process, which is definitely contributing to the improvement of the Ni@C HER activity. Furthermore, the bulk electrolysis data was obtained by measuring total charge generated as a function of time as presented in Fig. 5**d**. The trend reinforces the observed HER activity in LSV with Ni@C showing the best catalytic performance.

It is well-known that the double layer capacitance (C_{dl}) is proportional to the real electrochemical surface area (ECSA) and, in turn, to the number of electrocatalytic active sites [62]. To gain insights on the intrinsic catalytic activity of the MOF-derived nanoparticles, we have plotted the difference of anodic and cathodic current density against the scan rate at a non-faradaic potential of 0.15 V vs RHE as seen in Fig. 5**e.** The slope (C_{dl}) as well as the ECSA obtained for the Ni@C nanoparticles is almost twice times higher compared with the rest of the nanoparticles

revealing the larger number of catalytic active centers at the Ni electrochemical interfaces as well as its superior intrinsic catalytic performance (**Table S2**). In this sense, although the BET surface area of the Ni@C is lower compared with Co@C and even Cu@C, the TEM images have shown that Ni particles are well-dispersed into the carbon matrix while the other metals are forming agglomerated clusters at some extent (**See** Fig. 2**(a–d)**), which could facilitate the migration of reactants and electrolytes from the porous carbon network toward the active sites at the metal/carbon interfaces, thus boosting the HER electrocatalytic intrinsic yields. These findings were also supported by both the larger RF value and the smaller onset potential of the ECSA-normalized LSV of the Ni@C nanoparticles **(**Fig. 5**f and Table S2)**. Additionally, mass activity and specific activity constitute a key performance metric to compare different catalysts [63]. In this sense, Ni@C catalyst significantly surpassed the other samples in both mass and specific activities (Fig. 5g), demonstrating that the HER catalytic processes are most efficient on Ni@C active sites.

To unravel the influence of the carbonization temperatures over the HER electrocatalytic behavior of the as-synthesized Ni@C we have obtained the polarization curves of the Ni@C nanocatalysts obtained at 500 °C, 700 °C and 800 °C using the same experimental conditions as seen Fig. 5**h**. The onset potential of the Ni@C nanocatalyst prepared at 600 °C (-0.087 V) outperformed the values of -0.159 V, -0.237 V and -0.270 V obtained for the nanomaterials synthesized at 500 °C, 700 °C and 800 °C, respectively. To understand this phenomenon, we have carried out the XRD and TEM analysis of the nanocatalysts and the results are presented in **Fig. S8 and Fig. S9 (a–c)**. XRD analysis confirmed the presence of metallic nickel in the samples. Furthermore, TEM analysis revealed that the particle size increases with increasing carbonization temperature and this is due to the fact that the higher temperature favors faster nucleation of the particles resulting higher agglomeration of the particles. The decreased activity might be attributed to both the agglomeration of the metallic nanoparticles as well as the appearance of ineffective interconnected carbon network pathways that can negatively influence the ion transport processes across the framework and in turn suppress the number of the active sites.

The stability of the as-prepared Ni@C in acidic medium was further investigated using chronoamperometric measurements. As observed in Fig. 5i, the Ni@C nanocatalyst was found to be electrocatalytically active even after 20 h of operation indicating its excellent long-term stabilities properties. It can be significantly attributed to the protective action of the carbon shell which avoid the degradation and the aggregation of the Ni nanoparticles preserving their HER activity for a long time. Also, the cyclic stability of Ni@C electrocatalyst was investigated by LSV after 500 scans. It can be seen that there is only a negligible change in the current densities between the initial scan and the scan after 500 cycles (Fig. 5**i: inset**). In summary, the impressive HER catalytic performance of Ni@C nanoparticles is strongly connected with their unique structural properties which provide a large number of electrocatalytically active sites and fast mass transport channels to speed up the kinetic of the electrocatalytic reactions.

Conclusion

In this work, MOF derived transition metal nanoparticles (Cu, Ni, Fe and Co) embedded on porous carbon were successfully synthesized from MOF precursors using a facile carbonization method. The as-synthesized MOF derived M@C nanocatalysts were used for the first time as a Fenton-like catalyst to activate peroxymonosulfate for the degradation of organic pollutants as well as electrocatalysts for HER reaction. The Co@C was found to be the best, environmentally benign and effective heterogeneous nanocatalyst for the degradation of methylene blue via PMS activation. Radical quenching tests demonstrated that the sulfate radicals are the main reactive radical species for the MB degradation by PMS/Co@C system. Mechanistic study demonstrated that the cycle of Co (II)–Co(III)–Co(II) was mainly responsible for producing active radicals through PMS activation for the dye degradation confirming that the outstanding catalytic activity of the M@C nanocatalysts could be ascribed to the synergetic effect rising from the metal nanoparticles and the porous carbon network. Finally, the as-prepared Co@C nanocatalyst displayed superior catalytic activity and stability after four cycles. As energy-conversion material, the as-synthesized Ni@C catalysts demonstrated promising HER performances. They exhibited a remarkable electrocatalytic activity toward the electrochemical generation of H_2 rendering an onset overpotential of 61 mV, Tafel slope of 82 mV·dec^{-1} and a longtime stability of about 20 h, which is comparable with the most efficient Ni-based HER catalysts. This remarkable behavior is mainly attributed to the large number of electrocatalytically active sites and fast mass transport channels along the porous carbon encapsulated metal nanoparticles framework, which significantly improved the kinetic of the electrocatalytic reactions. In brief, this work opens up new avenues for the design and fabrication of novel and low-cost multifunctional carbon encapsulated transition metal nanocatalysts for both environmental and energy applications.

Declaration of Competing Interest

The authors declare that they have no known competing financial interests or personal relationships that could have appeared to influence the work reported in this paper..

CRediT authorship contribution statement

Md Ariful Ahsan: Conceptualization, Methodology, Investigation, Writing - original draft. **Alain R. Puente Santiago:** Methodology. **Aruna Narayanan Nair:** Methodology. **J. Mark Weller:** Resources. **Mohammed F. Sanad:** Methodology. **Delia J. Valles-Rosales:** Resources. **Candace K. Chan:** Resources. **Sreeprasad Sreenivasan:** Writing - review & editing, Supervision. **Juan C. Noveron:** Conceptualization, Project administration, Funding acquisition, Supervision.

Acknowledgments

This project was supported by the US National Science Foundation (NSF) Nanotechnology-Enabled Water Treatment Center (NEWT ERC435 1449500) (to J.C.N.), the USDA2019-38422-30214 (to J.C.N.). SS acknowledges the support through UTEP start-up, UT STARs, URI funding, and NSF-PREM grant #DMR-1827745.

Appendix A. Supplementary data

Supplementary material related to this article can be found, in the online version, at doi:https://doi.org/10.1016/j.mcat.2020.111241.

References

[1] K. Xie, H. Zhang, S. Sun, Y. Gao, Functions of boric acid in fabricating TiO_2 for photocatalytic degradation of organic contaminants and hydrogen evolution, Mol. Catal. 479 (2019), 110614.
[2] N. Dominguez, B. Torres, L.A. Barrera, J.E. Rincon, Y. Lin, R.R. Chianelli, M. A. Ahsan, J.C. Noveron, Bimetallic CoMoS composite anchored to biocarbon fibers as a high-capacity anode for Li-Ion batteries, ACS Omega 3 (2018) 10243–10249.
[3] M. Nasrollahzadeh, N. Shafiei, Z. Nezafat, N.S.S. Bidgoli, Recent progresses in the application of lignin derived (nano) catalysts in oxidation reactions, Mol. Catal. 489 (2020), 110942.
[4] M.T. Islam, R. Saenz-Arana, C. Hernandez, T. Guinto, M.A. Ahsan, H. Kim, Y. Lin, B. Alvarado-Tenorio, J.C. Noveron, Adsorption of methylene blue and tetracycline onto biomass-based material prepared by sulfuric acid reflux, RSC Adv. 8 (2018) 32545–32557.
[5] M.T. Islam, A.G. Hyder, R. Saenz-Arana, C. Hernandez, T. Guinto, M.A. Ahsan, B. Alvarado-Tenorio, J.C. Noveron, Removal of methylene blue and tetracycline from water using peanut shell derived adsorbent prepared by sulfuric acid reflux, J. Environ. Chem. Eng. 7 (2019), 102816.
[6] M.Y. Akram, M.U. Hameed, N. Akhtar, S. Ali, I. Maitlo, X.-Q. Zhu, N. Jun, Synthesis of high performance Ni3C-Ni decorated thermally expanded reduced graphene oxide (TErGO/Ni_3C-Ni) nanocomposite: a stable catalyst for reduction of Cr (VI) and organic dyes, J. Hazard. Mater. 366 (2019) 723–731.

[7] M.A. Ahsan, A.R. Puente Santiago, A. Rodriguez, V. Maturano-Rojas, B. Alvarado-Tenorio, R. Bernal, J.C. Noveron, Biomass-derived ultrathin carbon-shell coated iron nanoparticles as high-performance tri-functional HER, ORR and Fenton-like catalysts, J. Clean. Prod. (2020) 124141, https://doi.org/10.1016/j.jclepro.2020.124141.

[8] Z.-z. Yang, C. Zhang, G.-m. Zeng, X.-f. Tan, H. Wang, D.-l. Huang, K.-h. Yang, J.-j. Wei, C. Ma, K. Nie, Design and engineering of layered double hydroxide based catalysts for water depollution by advanced oxidation processes: a review, J. Mater. Chem. A. 8 (2020) 4141–4173.

[9] P. Hu, M. Long, Cobalt-catalyzed sulfate radical-based advanced oxidation: a review on heterogeneous catalysts and applications, Appl. Catal. B Environ. 181 (2016) 103–117.

[10] W. Ma, N. Wang, Y. Du, T. Tong, L. Zhang, K.-Y.A. Lin, X. Han, One-step synthesis of novel Fe_3C@ nitrogen-doped carbon nanotubes/graphene nanosheets for catalytic degradation of Bisphenol A in the presence of peroxymonosulfate, Chem. Eng. J. 356 (2019) 1022–1031.

[11] A. Takdastan, B. Kakavandi, M. Azizi, M. Golshan, Efficient activation of peroxymonosulfate by using ferroferric oxide supported on carbon/UV/US system: a new approach into catalytic degradation of bisphenol A, Chem. Eng. J. 331 (2018) 729–743.

[12] Z. Chen, X. Duan, W. Wei, S. Wang, B.-J. Ni, Recent advances in transition metal-based electrocatalysts for alkaline hydrogen evolution, J. Mater. Chem. A. 7 (2019) 14971–15005.

[13] S. Wen, T. Yang, N. Zhao, L. Ma, E. Liu, Ni-Co-Mo-O nanosheets decorated with NiCo nanoparticles as advanced electrocatalysts for highly efficient hydrogen evolution, Appl. Catal. B Environ. 258 (2019), 117953.

[14] L. Jin, X. Zhao, J. Ye, X. Qian, M. Dong, MOF-derived magnetic Ni-carbon submicrorods for the catalytic reduction of 4-nitrophenol, Catal. Commun. 107 (2018) 43–47.

[15] Y. Yang, X. Li, F. Yang, W. Zhang, X. Zhang, Y. Ren, New route toward integrating large nickel nanocrystals onto mesoporous carbons, Appl. Catal. B Environ. 165 (2015) 94–102.

[16] J. Kang, R. Han, J. Wang, L. Yang, G. Fan, F. Li, In situ synthesis of nickel carbide-promoted nickel/carbon nanofibers nanocomposite catalysts for catalytic applications, Chem. Eng. J. 275 (2015) 36–44.

[17] J. Zhang, H. Zhao, J. Li, H. Jin, X. Yu, Y. Lei, S. Wang, In situ encapsulation of Iron complex nanoparticles into biomass-derived heteroatom-enriched carbon nanotubes for high-performance supercapacitors, Adv. Energy Mater. 9 (2019), 1803221.

[18] A.K. Haridas, J. Jeon, J. Heo, Y. Liu, R. Saroha, J.H. Joo, H.-J. Ahn, K.-K. Cho, J.-H. Ahn, In-situ construction of Iron sulfide nanoparticle loaded graphitic carbon capsules from waste biomass for sustainable lithium-ion storage, ACS Sustainable Chem. Eng. 7 (2019) 6870–6879.

[19] A.B. Kanj, R. Verma, M. Liu, J. Helfferich, W. Wenzel, L. Heinke, Bunching and immobilization of ionic liquids in nanoporous metal–Organic framework, Nano Lett. 19 (2019) 2114–2120.

[20] M.A. Ahsan, V. Jabbari, M.T. Islam, R.S. Turley, N. Dominguez, H. Kim, E. Castro, J.A. Hernandez-Viezcas, M.L. Curry, J. Lopez, J.L. Gardea-Torresdey, J.C. Noveron, Sustainable synthesis and remarkable adsorption capacity of MOF/graphene oxide and MOF/CNT based hybrid nanocomposites for the removal of Bisphenol A from water, Sci. Total Environ. 673 (2019) 306–317.

[21] X. Wang, P. Zhou, G. Qiu, X. Zhang, L. Wang, Q. Zhang, M. Wang, Z. Liu, Excellent electromagnetic wave absorption properties of porous core-shell CoO/Co@ C nanocomposites derived from a needle-shaped $Co(OH)_2$@ ZIF-67 template, J. Alloys. Compd. 842 (2020), 155807.

[22] Y. Li, Y. Xu, W. Yang, W. Shen, H. Xue, H. Pang, MOF-derived metal oxide composites for advanced electrochemical energy storage, Small 14 (2018), 1704435.

[23] A.R. Puente Santiago, O. Fernandez-Delgado, A. Gomez, M.A. Ahsan, L. Echegoyen, Fullerenes as key components for low-dimensional (photo)electrocatalytic nanohybrid materials, Angew. Chem. Int. Ed. (2020), https://doi.org/10.1002/anie.202009449.

[24] D. Rodriguez-Padron, M.A. Ahsan, M.F. Sanad, R. Luque, A.R.P. Santiago, Proteins-based nanocatalysts for energy conversion reactions, Top. Curr. Chem. 378 (2020) 43.

[25] H. Kim, A. Renteria-Marquez, M.D. Islam, L.A. Chavez, C.A. Garcia Rosales, M. A. Ahsan, T.L. Bill Tseng, N.D. Love, Y. Lin, Fabrication of bulk piezoelectric and dielectric $BaTiO_3$ ceramics using paste extrusion 3D printing technique, J. Am. Ceram. Soc. 102 (2019) 3685–3694.

[26] M.J. Muñoz-Batista, D. Rodríguez-Padrón, A.R. Puente-Santiago, A. Kubacka, R. Luque, M. Fernández-García, Sunlight-driven hydrogen production using an annular flow photoreactor and g-C3N4-Based catalysts, Chem. Photo. Chem. 2 (2018) 870–877.

[27] A. Franco, M. Cano, J.J. Giner-Casares, E. Rodríguez-Castellón, R. Luque, A. R. Puente-Santiago, Boosting the electrochemical oxygen reduction activity of hemoglobin on fructose@ graphene-oxide nanoplatforms, Chem. Commun. (Camb.) 55 (2019) 4671–4674.

[28] J. Zhou, Y. Dou, A. Zhou, R.M. Guo, M.J. Zhao, J.R. Li, MOF template-directed fabrication of hierarchically structured electrocatalysts for efficient oxygen evolution reaction, Adv. Energy Mater. 7 (2017), 1602643.

[29] M.A. Ahsan, V. Jabbari, M.A. Imam, E. Castro, H. Kim, M.L. Curry, D.J. Valles-Rosales, J.C. Noveron, Nanoscale nickel metal organic framework decorated over graphene oxide and carbon nanotubes for water remediation, Sci. Total Environ. 698 (2020), 134214.

[30] M.A. Ahsan, A.R. Puente Santiago, Y. Hong, N. Zhang, M. Cano, E. Rodriguez-Castellon, L. Echegoyen, S.T. Sreenivasan, J.C. Noveron, Tuning of tri-functional NiCu bimetallic nanoparticles confined in a porous carbon network with surface composition and local structural distortions for the electrocatalytic oxygen reduction, oxygen and hydrogen evolution reactions, J. Am. Chem. Soc. 142 (2020) 14688–14701.

[31] M.F. Sanad, A.E. Shalan, S.M. Bazid, E.S.A. Serea, E.M. Hashem, S. Nabih, M. A. Ahsan, A graphene gold nanocomposite-based 5-FU drug and the enhancement of the MCF-7 cell line treatment, RSC Adv. 9 (2019) 31021–31029.

[32] M.F. Sanad, E.S.A. Serea, S.M. Bazid, S. Nabih, M.A. Ahsan, A.E. Shalan, High cytotoxic activity of ZnO@ leucovorin nanocomposite-based materials against an MCF-7 cell model, Anal. Methods 12 (2020) 2176–2184.

[33] M.A. Ahsan, V. Jabbari, A.A. El-Gendy, M.L. Curry, J.C. Noveron, Ultrafast catalytic reduction of environmental pollutants in water via MOF-derived magnetic Ni and Cu nanoparticles encapsulated in porous carbon, Appl. Surf. Sci. 497 (2019), 143608.

[34] S. RK, B. Gangadhar, H. Basu, V. Manisha, N. GRK, R. AVR, Remediation of malathion contaminated soil using zero valent iron nano-particles, Am. J. Anal. Chem. 3 (2012) 76–82.

[35] M.A. Ahsan, E. Deemer, O. Fernandez-Delgado, H. Wang, M.L. Curry, A.A. El-Gendy, J.C. Noveron, Fe nanoparticles encapsulated in MOF-derived carbon for the reduction of 4-nitrophenol and methyl orange in water, Catal. Commun. 130 (2019), 105753.

[36] M.A. Ahsan, O. Fernandez-Delgado, E. Deemer, H. Wang, A.A. El-Gendy, M. L. Curry, J.C. Noveron, Carbonization of Co-BDC MOF results in magnetic C@ Co nanoparticles that catalyze the reduction of methyl orange and 4-nitrophenol in water, J. Mol. Liq. 290 (2019), 111059.

[37] A.C. Ferrari, J. Robertson, Interpretation of Raman spectra of disordered and amorphous carbon, Phys. Rev. B 61 (2000) 14095–14107.

[38] J. Gong, J. Liu, L. Ma, X. Wen, X. Chen, D. Wan, H. Yu, Z. Jiang, E. Borowiak-Palen, T. Tang, Effect of Cl/Ni molar ratio on the catalytic conversion of polypropylene into Cu–Ni/C composites and their application in catalyzing "Click" reaction, Appl. Catal. B Environ. 117 (2012) 185–193.

[39] Y. Li, G. Hou, J. Yang, J. Xie, X. Yuan, H. Yang, M. Wang, Facile synthesis of MOF 235 and its superior photocatalytic capability under visible light irradiation, RSC Adv. 6 (2016) 16395–16403.

[40] X. Zheng, X. Han, H. Liu, J. Chen, D. Fu, J. Wang, C. Zhong, Y. Deng, W. Hu, Controllable synthesis of Ni x Se ($0.5 \leq x \leq 1$) nanocrystals for efficient rechargeable zinc–air batteries and water splitting, ACS Appl. Mater. Interfaces 10 (2018) 13675–13684.

[41] B. Chen, F. Li, Z. Huang, G. Yuan, Carbon-coated Cu-Co bimetallic nanoparticles as selective and recyclable catalysts for production of biofuel 2, 5-dimethylfuran, Appl. Catal. B Environ. 200 (2017) 192–199.

[42] A. Yousef, N.A. Barakat, M.H. El-Newehy, M. Ahmed, H.Y. Kim, Catalytic hydrolysis of ammonia borane for hydrogen generation using Cu(0) nanoparticles supported on TiO_2 nanofibers, Colloid. Surf. A Physicochem. Eng. Asp. 470 (2015) 194–201.

[43] Y.-H. Guan, J. Ma, Y.-M. Ren, Y.-L. Liu, J.-Y. Xiao, L.-q. Lin, C. Zhang, Efficient degradation of atrazine by magnetic porous copper ferrite catalyzed peroxymonosulfate oxidation via the formation of hydroxyl and sulfate radicals, Water Res. 47 (2013) 5431–5438.

[44] Y. Lei, C.-S. Chen, Y.-J. Tu, Y.-H. Huang, H. Zhang, Heterogeneous degradation of organic pollutants by persulfate activated by CuO-Fe_3O_4: mechanism, stability, and effects of pH and bicarbonate ions, Environ. Sci. Technol. 49 (2015) 6838–6845.

[45] R. Sharma, V. Kumar, S. Bansal, S. Singhal, Assortment of magnetic nanospinels for activation of distinct inorganic oxidants in photo-Fenton's process, J. Mol. Catal. A Chem. 402 (2015) 53–63.

[46] G.P. Anipsitakis, D.D. Dionysiou, Radical generation by the interaction of transition metals with common oxidants, Environ. Sci. Technol. 38 (2004) 3705–3712.

[47] T.B. Nguyen, R.-a. Doong, C. Huang, C.-W. Chen, C.-D. Dong, Activation of persulfate by CoO nanoparticles loaded on 3D mesoporous carbon nitride (CoO@ meso-CN) for the degradation of methylene blue (MB), Sci. Total Environ. 675 (2019) 531–541.

[48] D.L. Ball, J.O. Edwards, The kinetics and mechanism of the decomposition of Caro's acid, I, J. Am. Chem. Soc. 78 (1956) 1125–1129.

[49] F. Ghanbari, C.A. Martínez-Huitle, Electrochemical advanced oxidation processes coupled with peroxymonosulfate for the treatment of real washing machine effluent: a comparative study, J. Electroanal. Chem. Lausanne (Lausanne) 847 (2019), 113182.

[50] Y. Yao, C. Xu, J. Qin, F. Wei, M. Rao, S. Wang, Synthesis of magnetic cobalt nanoparticles anchored on graphene nanosheets and catalytic decomposition of orange II, Ind. Eng. Chem. Res. 52 (2013) 17341–17350.

[51] M.A. Ahsan, A.R. Puente Santiago, M.F. Sanad, J. Mark Weller, O. Fernandez-Delgado, L.A. Barrera, V. Maturano-Rojas, B. Alvarado-Tenorio, C.K. Chan, J. C. Noveron, Tissue paper-derived porous carbon encapsulated transition metal nanoparticles as advanced non-precious catalysts: carbon-shell influence on the electrocatalytic behaviour, J. Colloid Interface Sci. (2020), https://doi.org/10.1016/j.jcis.2020.08.012.

[52] Y. Pi, L. Ma, P. Zhao, Y. Cao, H. Gao, C. Wang, Q. Li, S. Dong, J. Sun, Facile green synthetic graphene-based Co-Fe Prussian blue analogues as an activator of peroxymonosulfate for the degradation of levofloxacin hydrochloride, J. Colloid Interf. Sci. 526 (2018) 18–27.

[53] N.S. Shah, J.A. Khan, M. Sayed, Z.U.H. Khan, H.S. Ali, B. Murtaza, H.M. Khan, M. Imran, N. Muhammad, Hydroxyl and sulfate radical mediated degradation of ciprofloxacin using nano zerovalent manganese catalyzed $S_2O_8^{2-}$, Chem. Eng. J. 356 (2019) 199–209.

[54] J. Liu, D. Zhu, C. Guo, A. Vasileff, S.Z. Qiao, Design strategies toward advanced MOF-derived electrocatalysts for energy-conversion reactions, Adv. Energy Mater. 7 (2017), 1700518.
[55] S. Dang, Q.-L. Zhu, Q. Xu, Nanomaterials derived from metal–organic frameworks, Nat. Rev. Mater. 3 (2017) 1–14.
[56] T. Qiu, Z. Liang, W. Guo, H. Tabassum, S. Gao, R. Zou, Metal–Organic framework-based materials for energy conversion and storage, ACS Energy Lett. 5 (2020) 520–532.
[57] Y. Yan, B. Xia, Z. Xu, X. Wang, Recent development of molybdenum sulfides as advanced electrocatalysts for hydrogen evolution reaction, ACS Catal. 4 (2014) 1693–1705.
[58] D. Alba-Molina, A.R.P. Santiago, J.J. Giner-Casares, E. Rodríguez-Castellón, M. T. Martín-Romero, L. Camacho, R. Luque, M. Cano, Tailoring the ORR and HER electrocatalytic performances of gold nanoparticles through metal–ligand interfaces, J. Mater. Chem. A. 7 (2019) 20425–20434.
[59] X. Xiao, Y. Wang, X. Xu, T. Yang, D. Zhang, Preparation of the flower-like MoS_2/SnS_2 heterojunction as an efficient electrocatalyst for hydrogen evolution reaction, Mol. Catal. 487 (2020), 110890.
[60] Y. He, R. Cui, C. Gao, J. Zhang, X.A. Li, Cobalt phosphide microspheres integrated with cadmium sulfide nanowires as an efficient photocatalyst for hydrogen evolution reaction, Mol. Catal. 469 (2019) 161–166.
[61] M.A. Ahsan, M.A. Imam, A.R. Puente Santiago, A. Rodriguez, B. Alvarado-Tenorio, R.A. Bernal, R. Luque, J.C. Noveron, Spent tea leaves templated synthesis of highly active and durable cobalt-based trifunctional versatile electrocatalysts for hydrogen and oxygen evolution as well as oxygen reduction reactions, Green Chem. (2020), https://doi.org/10.1039/D0GC02155E.
[62] T. Kou, S. Wang, J.L. Hauser, M. Chen, S.R. Oliver, Y. Ye, J. Guo, Y. Li, Ni foam-supported Fe-doped β-Ni (OH) 2 nanosheets show ultralow overpotential for oxygen evolution reaction, ACS Energy Lett. 4 (2019) 622–628.
[63] Z. Chen, W. Gong, Z. Liu, S. Cong, Z. Zheng, Z. Wang, W. Zhang, J. Ma, H. Yu, G. Li, Coordination-controlled single-atom tungsten as a non-3d-metal oxygen reduction reaction electrocatalyst with ultrahigh mass activity, Nano Energy 60 (2019) 394–403.